Chinese Journal of Natural Medicines

Novel phenanthrene/bibenzyl trimers from the tubers of *Bletilla striata* attenuate neuroinammation *via* inhibition of NF-κB signaling pathway

Siyuan SHAO, Mohan SUN, Xianjie MA, Jianwei JIANG, Jinying TIAN, Jianjun ZHANG, Fei YE, Shuai LI

Citation: Siyuan SHAO, Mohan SUN, Xianjie MA, Jianwei JIANG, Jinying TIAN, Jianjun ZHANG, Fei YE, Shuai LI, Novel phenanthrene/bibenzyl trimers from the tubers of *Bletilla striata* attenuate neuroinammation *via* inhibition of NF-κB signaling pathway, Chinese Journal of Natural Medicines, 2024, 22(5), 441-454. doi: 10.1016/S1875-5364(24)60641-2.

View online: https://doi.org/10.1016/S1875-5364(24)60641-2

Available online at www.sciencedirect.com
ScienceDirect
Chinese Journal of Natural Medicines 2024, **22**(5): 441-454
doi: 10.1016/S1875-5364(24)60641-2
Chinese Journal of Natural Medicines

•Original article•

Novel phenanthrene/bibenzyl trimers from the tubers of *Bletilla striata* attenuate neuroinflammation *via* inhibition of NF-κB signaling pathway

SHAO Siyuan[Δ], SUN Mohan[Δ], MA Xianjie, JIANG Jianwei, TIAN Jinying, ZHANG Jianjun, YE Fei, LI Shuai[*]

State Key Laboratory of Bioactive Substance and Function of Natural Medicines, Institute of Materia Medica, Chinese Academy of Medical Sciences and Peking Union Medical College, Beijing 100050, China

Available online 20 May, 2024

[ABSTRACT] Five novel (9,10-dihydro) phenanthrene and bibenzyl trimers, as well as two previously identified biphenanthrenes and bibenzyls, were isolated from the tubers of *Bletilla striata*. Their structures were elucidated through comprehensive analyses of NMR and HRESIMS spectroscopic data. The absolute configurations of these compounds were determined by calculating rotational energy barriers and comparison of experimental and calculated ECD curves. Compounds **5b** and **6** exhibited inhibitory effects on LPS-induced NO production in BV-2 cells, with IC_{50} values of 12.59 ± 0.40 and 15.59 ± 0.83 μmol·L^{-1}, respectively. A mechanistic study suggested that these compounds may attenuate neuroinflammation by reducing the activation of the AKT/IκB/NF-κB signaling pathway. Additionally, compounds **3a**, **6**, and **7** demonstrated significant PTP1B inhibitory activities, with IC_{50} values of 1.52 ± 0.34, 1.39 ± 0.11, and 1.78 ± 0.01 μmol·L^{-1}, respectively. Further investigation revealed that compound **3a** might inhibit LPS-induced PTP1B overexpression and NF-κB activation, thereby mitigating the neuroinflammatory response in BV-2 cells.

[KEY WORDS] *Bletilla striata*; Phenanthrene/bibenzyl trimer; NO inhibition; AKT/IκB/NF-κB signaling pathway; PTP1B inhibitory effect

[CLC Number] R965 **[Document code]** A **[Article ID]** 2095-6975(2024)05-0441-14

Introduction

Neuroinflammation is widely recognized as a defining feature of various neurodegenerative diseases, including Alzheimer's disease, Parkinson's disease, and Huntington's disease [1]. Lipopolysaccharide (LPS)-induced activation of microglia leads to the excessive release of inflammatory mediators such as inducible nitric oxide synthase (iNOS), tumor necrosis factor-alpha (TNF-α), and interleukin-1 beta (IL-1β), contributing to neuronal damage [2]. Substantial evidence indicates that nuclear factor kappa-B (NF-κB) plays a central role in regulating the expression of pro-inflammatory factors in activated microglia [3]. AKT, serving as an upstream regulator of NF-κB, is activated by LPS, facilitating the phosphorylation of the NF-κB inhibitor (IκB), thereby activating NF-κB [4, 5]. Additionally, protein tyrosine phosphatase 1B (PTP1B), traditionally known as a negative regulator of the insulin signaling pathway, has emerged as a positive regulator in neuroinflammation [6–8]. LPS-induced overexpression of PTP1B in microglial cells can exacerbate the neuroinflammatory response by activating NF-κB, leading to an increased release of pro-inflammatory factors [6]. This evidence suggests that inhibiting the NF-κB signaling pathway could be a viable therapeutic strategy to mitigate neuroinflammation.

Natural products have emerged as crucial sources for drug discovery, offering diverse bioactivity and unique structures [9]. *Bletilla striata*, a medicinal herb from the Orchidaceae family, is widely distributed across northern Myanmar, China, and Japan. Its tubers have been traditionally used in Chinese medicine to treat a variety of conditions including hemoptysis, wounds, ulcers, pyogenic infections, and chapped skin [10]. Phytochemical studies have identified several types of compounds in *B. striata,* including bibenzyls [11], phenanthrenes [11], flavones [12], triterpenes [13], and steroids [14]. Pharmacological research has demonstrated that

[Received on] 02-Oct.-2023
[Research funding] This research was supported by the National Natural Science Foundation of China (No. 81903488) and the CAMS Innovation Fund for Medical Sciences (No. CIFMS-2021-I2M-1-026).
[*Corresponding author] E-mail: lishuai@imm.ac.cn
[Δ]These authors contributed equally to this work.
These authors have no conflict of interest to declare.

these constituents possess anti-inflammatory [14], anti-bacterial [15], and cytotoxic activities [16]. The goal of this research was to identify novel and bioactive compounds from the tubers of *B*. *striata*. Consequently, five new phenanthrene/bibenzyl trimers and two known phenanthrene derivatives were discovered. Their anti-neuroinflammatory activities and the mechanisms underlying these effects were explored following the structural elucidation of these compounds.

Experimental

General experimental procedure

Optical rotations were measured using a Rudolph Research Autopol V automatic polarimeter. UV spectra were recorded on a JASCO J-650 ultraviolet spectrometer, and IR spectra on a Nicolet iS10 FTIR spectrometer. ECD spectra were obtained with a JASCO J-815 circular dichroism spectrometer. High-resolution electrospray ionization mass spectrometry (HRESIMS) data were acquired using an Agilent 6520 Accurate-Mass Q-TOF LC/MS. NMR spectra were recorded on Bruker AVANCE III 600 MHz spectrometers, with chemical shifts reported in δ (ppm) relative to tetramethylsilane (TMS) as the internal standard. High-performance liquid chromatography (HPLC) analyses were performed on a Shimadzu LC-6AD system equipped with a Shimadzu SPD-20A UV-VIS detector and an YMC-Pack Ph column (10.0 mm × 250 mm, 5 μm particle size). Chiral-phase HPLC experiments utilized a CHIRALPAK IA column (4.6 mm × 250 mm, 5 μm particle size).

Plant material

The tubers of *Bletilla striata* were collected in Kunming, Yunnan Province, China, in May 2013. The plant material was identified by Professor MA Lin and the specimen (ID-S-2766) was conserved in herbarium of Institute of Materia Medica, Chinese Academy of Medical Sciences and Peking Union Medical College.

Extraction and isolation

The dried tubers of *Bletilla striata* (40 kg) were extracted by 90% ethanol twice to yield the crude extract (1.4 kg). The extract was dispersed in water and then extracted successively by petroleum ether and ethyl acetate. The ethyl acetate layer (400 g) was separated on a silica gel column, eluting with a gradient mixture of petroleum ether–actone (20 ∶ 15 ∶ 1, 2 ∶ 1, 1 ∶ 1) to produce fractions A–L.

Fraction I (28 g) was separated by a silica gel column and eluted with a gradient mixture of petroleum ether–ethyl acetate (4 ∶ 1–1 ∶ 1) to obtain fractions I1–I13. Frs. I5 and I6 were combined (3 g) and then separated by a sephadex LH-20 column with a mixture of petroleum ether–chloroform–methanol (5 ∶ 5 ∶ 1) to afford fractions I5a–I5h. Fr. I5h was purified by RP-C_{18} HPLC semi-preparation and eluted with CH_3OH–H_2O (55 ∶ 45) to yield compound **6** (7.0 mg, t_R = 28.1 min). Fr. I7 (2 g) was separated by a sephadex LH-20 column with a mixture of petroleum ether–chloroform–methanol (5 ∶ 5 ∶ 1) to afford fractions I7a–I7t. Fr. I7p was purified by HPLC preparation and eluted with CH_3OH–H_2O (60 ∶ 40) to yield compound **7** (7.0 mg, t_R = 27.3 min).

Fraction K (25 g) was chromatographed by a sillica gel column with a gradient mixture of CH_2Cl_2–CH_3OH (100 ∶ 1–10 ∶ 1) to obtain fractions K1–K8. Fr. K3 (3.6 g) was separated by an ODS column with a gradient mixture of CH_3OH–H_2O (40%–100%) to yield subfractions K3a–K3i. Fr. K3g was isolated by a sephadex LH-20 column with a mixture of CH_3OH–H_2O (60%–90%) to produce fractions K3g1–K3g17. Frs. K3g14 and K3g15 were combined and purified *via* RP-C18 HPLC semi-preparation with CH_3OH–H_2O (47 ∶ 53) to yield compound **4** (10 mg, t_R = 62.6 min). Compound **4** was isolated by chiral HPLC (*n*-hexane–isopropanol, 65 ∶ 35) to produce **4a** (4.2 mg, t_R = 12.5 min) and **4b** (3.7 mg, t_R = 18.6/24.3 min). Fr. K3h was separated by a sephadex LH-20 column with a mixture of CH_3OH–H_2O (60%–90%) to produce fractions K3h1–K3h23. Fr. K3h22 was purified through RP-C18 HPLC semi-preparation and eluted with CH_3CN–H_2O (50 ∶ 50) to furnish compound **3** (5.4 mg, t_R = 17.2 min). Compound **3** was further purified by chiral HPLC (*n*-hexane–isopropanol, 60 ∶ 40) to produce **3a** (2.6 mg, t_R = 6.3/7.1 min) and **3b** (2.4 mg, t_R = 19.4/21.0 min).

Fractions K4 and K5 were combined (6.6 g) and then separated by an ODS column with a gradient of CH_3OH–H_2O (40%–100%) to yield fractions K4a and K4b. Fr. K4a (1.7 g) was isolated by a sephadex LH-20 column using a mixture of CH_3OH–H_2O (60%–90%) to produce fractions K4a1–K4a17. Fr. K4a9 was purified by RP-C_{18} HPLC semi-preparation using CH_3OH–H_2O (63 ∶ 37) to yield compound **5** [**5I** (2 mg, t_R = 30.2 min) and **5II** (2 mg, t_R = 32.7 min)]. Fr. K4a11 was separated by RP-C18 HPLC with CH_3OH–H_2O (60 ∶ 40) to afford compounds **1** (3.5 mg, t_R = 47.3 min) and **2** (3.5 mg, t_R = 50.2 min). Compounds **1**, **2**, and **5** were further purified with chiral HPLC (*n*-hexane–isopropanol, 65:35) to produce **1a** (1.0 mg, t_R = 7.5/9.5 min), **1b** (0.5 mg, t_R = 12.4/18.5 min), **2a** (0.3 mg, t_R = 13.6/22.0 min), **2b** (0.4 mg, t_R = 25.9/63.0 min), **5a** (1.5 mg, t_R = 12.0/23.5 min), and **5b** (1.8 mg, t_R = 23.5/27.1 min).

Physicochemical and spectroscopic data of new compounds

*Blephebibnol F (**1**)*

Yellow amorphous powder; UV (CH_3OH) λ_{max} (log ε) 205 (4.93), 281 (4.57), 299 (4.45) nm; IR (Microscope) ν_{max} 3398, 2936, 2840, 1589, 1459, 1198 cm^{-1}; HR-ESI-MS *m/z* 725.2744 $[M + H]^+$ (Calcd. for $C_{45}H_{41}O_9$, 725.2745); ^1H and ^{13}C NMR data see Tables **1** and **2**.

(a*R*)-blephebibnol F (**1a**): $[\alpha]_D^{20}$ −7.0 (*c* 0.1, CH_3OH); ECD (CH_3OH) λ_{max} (Δε) 202 (+3.19), 228 (+1.36), 252 (−1.32), 281 (0.74), 317 (−0.43) nm.

(a*S*)-blephebibnol F (**1b**): $[\alpha]_D^{20}$ +6.0 (*c* 0.05, CH_3OH); ECD (CH_3OH) λ_{max} (Δε) 228 (−0.92), 251 (+1.20), 281 (−0.63), 313 (0.57) nm.

*Blephebibnol G (**2**)*

Yellow amorphous powder; UV (CH_3OH) λ_{max} (log ε) 205 (4.95), 281 (4.54), 296 (4.43) nm; IR (Microscope) ν_{max} 3351, 2923, 2851, 1591, 1460, 1209 cm^{-1}; HR-ESI-MS *m/z*

725.2742 [M + H]$^+$ (Calcd. for $C_{45}H_{41}O_9$, 725.2745); ^{1}H and ^{13}C NMR data see Tables **1** and **2**.

(a*R*)-blephebibnol G (**2a**): $[\alpha]_D^{20}$ −3.0 (*c* 0.1, CH_3OH); ECD (CH_3OH) λ_{max} (Δε) 220 (+1.47), 242 (−0.82), 270 (+1.10), 314 (−0.97) nm.

(a*S*)-blephebibnol G (**2b**): $[\alpha]_D^{20}$ +6.0 (*c* 0.05, CH_3OH); ECD (CH_3OH) λ_{max} (Δε) 221 (−3.47), 242 (+2.27), 269 (−2.99), 314 (+2.50) nm.

*Blephebibnol H (**3**)*

Yellow amorphous powder; UV (CH_3OH) λ_{max} (log ε) 211 (4.91), 218 (4.91), 280 (4.75), 299 (4.65) nm; IR (Microscope) ν_{max} 3503, 3407, 2922, 2850, 1589, 1462, 1210 cm^{-1}; HR-ESI-MS *m/z* 721.2451 [M − H]$^-$ (Calcd. for $C_{45}H_{37}O_9$, 721.2443); ^{1}H and ^{13}C NMR data see Tables **1** and **2**.

(a*R*)-blephebibnol H (**3a**): $[\alpha]_D^{20}$ −10.0 (*c* 0.08, CH_3OH); ECD (CH_3OH) λ_{max} (Δε) 224 (+9.95), 243 (−9.20), 270 (+12.97), 289 (−0.63), 315 (−9.39) nm.

(a*S*)-blephebibnol H (**3b**)**:** $[\alpha]_D^{20}$ +8.0 (*c* 0.08, CH_3OH); ECD (CH_3OH) λ_{max} (Δε) 223 (−7.32), 243 (+8.24), 270 (−10.90), 290 (+1.19), 314 (+8.39) nm.

*Blephebibnol I (**4**)*

Yellow amorphous powder; UV (CH_3OH) λ_{max} (log ε) 205 (4.74), 264 (4.64), 308 (4.12), 358 (3.63), 376 (3.68) nm; IR (Microscope) ν_{max} 3386, 2928, 2852, 1610, 1442, 1206 cm^{-1}; HR-ESI-MS *m/z* 717.2139 [M − H]$^-$ (Calcd. for $C_{45}H_{33}O_9$, 717.2130) ; ^{1}H and ^{13}C NMR data see Tables **1** and **2**.

(a*R*)-blephebibnol I (**4a**): $[\alpha]_D^{20}$ +17.0 (*c* 0.08, CH_3OH); ECD (CH_3OH) λ_{max} (Δε) 202 (+4.37), 230 (−2.03), 263 (+2.03), 285 (−0.69), 320 (−0.41), 370 (−0.36) nm.

(a*S*)-blephebibnol I (**4b**): $[\alpha]_D^{20}$ −19.0 (*c* 0.08, CH_3OH); ECD (CH_3OH) λ_{max} (Δε) 204 (−4.68), 230 (+2.75), 266 (−2.75), 285 (+0.87), 320 (+0.41), 372 (−0.54) nm.

*Blephebibnol J (**5**)*

5I: Yellow amorphous powder; UV (CH_3OH) λ_{max} (log ε) 203 (4.80), 260 (3.98), 281 (4.20), 300 (4.03), 311 (3.92) nm; IR (Microscope) ν_{max} 3375, 2934, 2842, 1590, 1458, 1194 cm^{-1}; HR-ESI-MS *m/z* 727.2899 [M + H]$^+$ (Calcd. for $C_{45}H_{43}O_9$, 727.2902); ^{1}H and ^{13}C NMR data see Tables **1** and **2**.

5II: Yellow amorphous powder; UV (CH_3OH) λ_{max} (log ε) 203 (4.65), 260 (3.93), 281 (4.04), 300 (3.89), 311 (3.79) nm; IR (Microscope) ν_{max} 3353, 2934, 2855, 1592, 1458, 1194 cm^{-1}; HR-ESI-MS *m/z* 727.2910 [M + H]$^+$ (Calcd. for $C_{45}H_{43}O_9$, 727.2902); ^{1}H and ^{13}C NMR data see Tables **1** and **2**.

(a*R*)-blephebibnol J (**5a**): $[\alpha]_D^{20}$ +6.0 (*c* 0.05, CH_3OH); ECD (CH_3OH) λ_{max} (*Δε*): 232 (−1.38), 255 (+0.78) nm.

(a*S*)-blephebibnol J (**5b**): $[\alpha]_D^{20}$ −3.0 (*c* 0.10, CH_3OH); ECD (CH_3OH) λ_{max} (*Δε*): 228 (+2.35), 252 (−0.92) nm.

Rotational energy barrier calculations

Conformational analysis was conducted on the Yinfo Cloud Platform (http://cloud.yinfotek.com) utilizing the Gentor software package [17]. The resulting conformers were optimized using the MMFF94 force field. For each compound, the conformer with the lowest energy was chosen as the initial geometry for a potential energy surface (PES) scan. Relaxed PES scans were carried out on selected dihedral angles through 360 steps, with incremental increases of 1 degree, employing redundant internal coordinates at the PM6 level.

ECD calculations

Structures for ECD calculations were optimized at the level of B3LYP/6-311G(d,p) in methanol [11]. Detailed methodology can be found in **Supporting Information**.

NO production inhibition in LPS-induced BV-2 cells

The inhibitory assay was conducted following the methodology described in our previous study [11]. BV-2 cells were cultured in DMEM supplemented with 10% fetal bovine serum (FBS), penicillin (100 U· mL^{-1}), and streptomycin (100 μg·mL^{-1}) in a controlled environment at 37 °C under a 5% CO_2 atmosphere. Subsequently, cells were seeded at a density of 5 × 10^4 cells/well in 96-well plates, using 100 μL of the cell suspension per well. The cells were then treated with various test samples for 4 h before being stimulated with LPS (2 μg·mL^{-1}) for 24 h, with some wells left unstimulated as controls. Griess reagent was added to the supernatants in equal volumes, and nitric oxide (NO) production was quantified by measuring the absorbance at 540 nm with a microplate reader. A standard curve was generated using $NaNO_2$ for quantification purposes. Additionally, cell viability was assessed using the MTT assay.

PTP1B inhibition in vitro

The assay to evaluate protein tyrosine phosphatase 1B (PTP1B) inhibition was conducted according to a previously described method [18]. Initially, a working buffer was prepared, comprising 34.5 mmol·L^{-1} MOPS, 1.9 mmol·L^{-1} DTT, 0.69 mmol·L^{-1} EDTA, 2.0 mg·mL^{-1} BSA, and 2 mol·L^{-1} NaCl. Subsequently, 10 μL of the test compounds and 10 μL of a PTP1B solution (12.5 mg·L^{-1}) were dispensed into each well of a 96-well plate, followed by the addition of 70 μL of the working buffer. The mixture was incubated at 37 °C for 15 min. Then, 10 μL of the substrate solution (pNPP at 100 mmol·L^{-1} in the working buffer) was added to each well and incubated for an additional 30 min. The reaction was terminated by introducing 100 μL of a 0.1 mol·L^{-1} Na_2CO_3 solution. The absorbance was measured at 405 nm using a Bio-Rad 680 microplate reader.

Molecular docking

Molecular docking calculations were executed using the Dock6 protocol on the Yinfo Cloud Computing Platform (https://cloud.yinfotek.com/). The three-dimensional (3D) structures of compounds **3a**, **6**, and **7**were prepared through energy minimization using the MMFF94 force field. The crystal structure of the PTP1B protein (PDB code: 4I8N, resolution: 2.50 Å) was retrieved from the RCSB Protein Data Bank (http://www.rcsb.org/). The binding pocket was defined based on the position of the crystal ligand. The DOCK 6.9 program [19, 20] was employed for semi-flexible docking, and the resulting poses were evaluated using the Grid scoring function.

Western blotting analysis

Protein expression analysis was conducted using West-

ern blotting assays [21]. BV-2 cells were seeded in 6-well plates at a density of 3 × 10^5 cells/well and incubated for 12 h. Subsequently, the cells were treated with various samples for 2 h. Curcumin (10 μmol·L^{-1}) and CinnGEL 2Me (10 μmol·L^{-1}) served as positive controls. Following treatment, the cells were lysed using RIPA buffer and proteins were extracted using protein extraction kits targeting NF-κB p65, phosphorylated NF-κB p65 (p-NF-κB p65), IκBα, phosphorylated IκBα (p-IκBα), AKT, phosphorylated AKT (p-AKT), and inducible nitric oxide synthase (iNOS) after LPS stimulation (2 μg·mL^{-1}) for 24 h. Proteins were quantified, loaded in equal amounts, and separated on a 10% SDS-PAGE, then transferred to polyvinylidene difluoride membranes. Glyceraldehyde 3-phosphate dehydrogenase (GAPDH) was utilized as an internal control. The UVP ChemStudio (Analytik Jena, USA) was employed for the quantitative analysis of band grayscale.

Quantitative real–time PCR (qRT–PCR) analysis

mRNA expression levels were determined by qRT-PCR assays [18]. BV-2 cells were cultured in 12-well plates at a density of 4 × 10^5 cells per well for 24 h, followed by treatment with LPS and various samples for an additional 24 h. Curcumin (10 μmol·L^{-1}) and CinnGEL 2Me (10 μmol·L^{-1}) were employed as positive controls. Total RNA was extracted using Trizol reagent, with its concentration measured at 260 nm using a spectrophotometer (Thermo Scientific, USA). Equal amounts of RNA (1 μg) were converted to cDNA using TransScript One-Step gDNA Removal and cDNA Synthesis SuperMix (TransGen Biotech, Beijing, China). qRT–PCR was performed over 40 cycles with TB Green Premix Ex TaqTM II (TaKaRa, Beijing, China), employing β-actin as the internal control. The primers used targeted iNOS, TNF-α, IL-1β, and β-actin. Analysis was conducted on a 7500 Fast Real-Time PCR system (Thermo Scientific, USA), with data processed using 7500 software v2.0.5.

Statistical analysis

The bioactive data were presented as the mean ± standard deviation (SD). Statistical analyses were conducted using one-way ANOVA through GraphPad Prism software v8.0.2. Differences in mean values were considered statistically significant if the *P* value was less than 0.05.

Results and Discussion

Compound **1** (Fig. 1) was obtained as a yellowish amorphous powder. Its molecular formula was established as $C_{45}H_{40}O_9$ based on HR-ESI-MS data, showing an ion peak at *m/z* 725.2744 $[M + H]^+$. The ^1H NMR spectrum (Table 1) revealed the presence of three aromatic protons at δ_H 6.55 (s, H-3), 7.94 (s, H-5), and 6.74 (s, H-8), two methylene groups at δ_H 2.56 (m, H_2-9) and 2.34 (m, H_2-10), and a methoxyl sig-

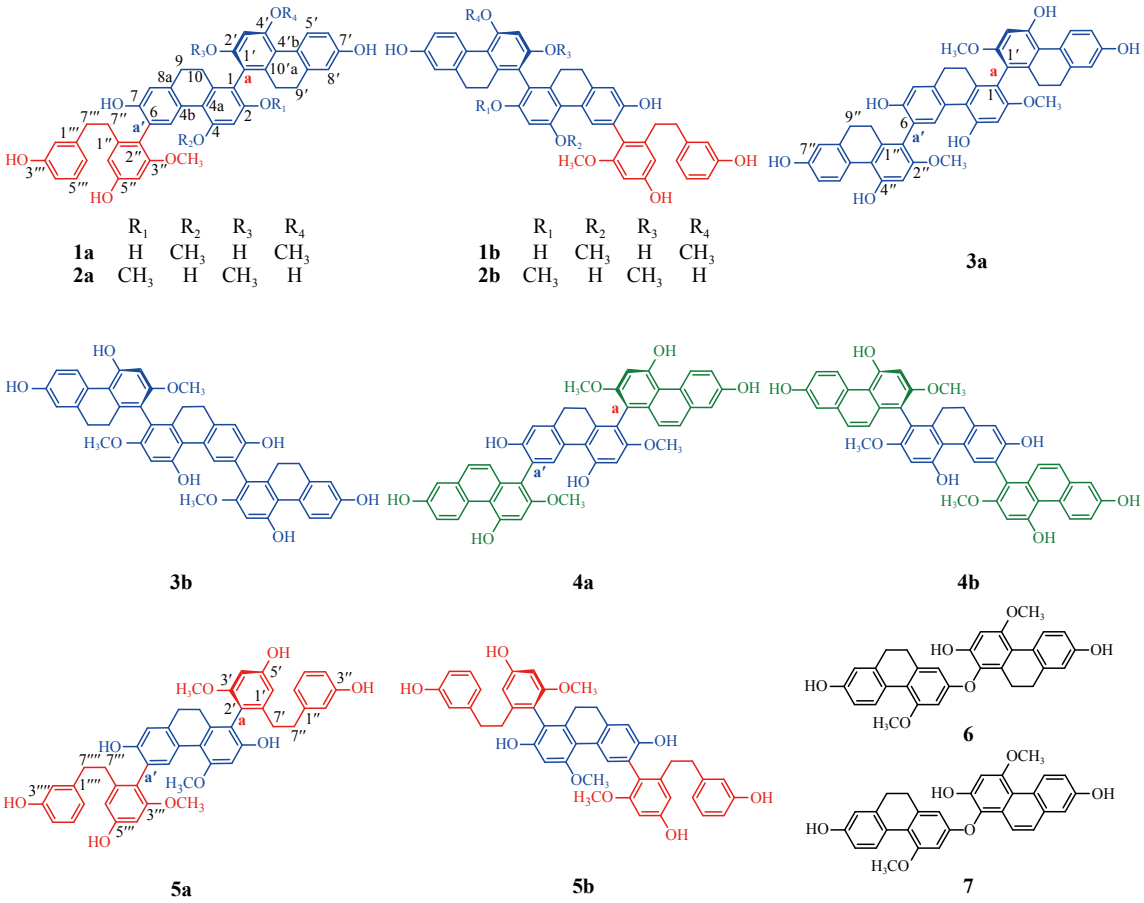

Fig. 1 Chemical structures of compounds 1–7.

nal at δ_H 3.82 (s, 4-OCH_3). HMBC correlations (Fig. 2) from H-3 to C-1 and C-4a, from H-5 to C-4a and C-8a, from H-8 to C-6 and C-9, from H_2-10 to C-1 and C-4a, and from 4-OCH_3 to C-4, coupled with ^{1}H-^{1}H COSY interactions between H_2-9 and H_2-10 (Fig. 2). NOESY correlations of 4-OCH_3 with H-3 and H-5 (Fig. 3), and the quaternary carbons at C-1 (δ_C 117.4) and C-6 (δ_C 122.2), indicated a 2,7-dihydroxy-4-methoxy-9,10-dihydrophenanthrene-1,6-yl structure. Additionally, the ^{1}H NMR data revealed a 2′,7′-dihydroxy-4′-methoxy-9′,10′-dihydroph-enanthrene-1′-ylmoiety by an aromatic singlet at δ_H 6.59 (H-3′, s), three AMX system proton signals at δ_H 8.05 (H-5′, d, J = 8.4), 6.644 (H-6′, dd, J = 8.4, 2.4), and 6.62 (H-8′, d, J = 2.4) , two methylenes at δ_H 2.56 (H_2-9′, m), 2.55 (m, H-10′), and 2.50 (m, H-10′), and a methoxyl signal at δ_H 3.89 (s, 4′-OCH_3). This was supported by HMBC correlations from H-3′ to C-1′ and C-4′a, from H-5′ to C-4′a and C-8′a, from H-6′ to C-4′b and C-8′, from H_2-9′ to C-4′b and C-8′, from H_2-10′ to C-1′ and C-4′a, and from 4′-OCH_3 to C-4′, alongside ^{1}H-^{1}H COSY interactions between H_2-9′ and H_2-10′, NOESY correlations of 4′-OCH_3 with H-3′ and H-5′, and the quaternary carbon at C-1′ (δ_C 116.6). Furthermore, the ^{1}H NMR spectrum exhibited additional signals indicative of a bibenzyl unit: two aromatic signals at δ_H 6.41 (d, J = 2.4 Hz, H-4″ and H-6″), four more aromatic signals at δ_H 6.40 (m, H-2‴), 6.51 (br d, J = 7.8 Hz, H-4‴), 6.95 (t, J = 7.8 Hz, H-5‴), and 6.41 (m, H-6‴), two methylenes at δ_H 2.58 (m, H_2-7″), 2.50 (m, H_2-7‴), and a methoxyl signal at δ_H 3.67 (s, 3″-OCH_3). This fragment was confirmed by HMBC cross-peaks from H-4″ to C-2″ and C-6″, from H-6″ to C-7″, from H-2‴ to C-4‴, C-6‴, and C-7‴, from H-5‴ to C-1‴ and C-3‴, from H-6‴ to C-7‴, and from 3″-OCH_3 to C-3″, together with the ^{1}H-^{1}H COSY correlation between H-7″ and H-7‴, the NOESY correlation of 3″-OCH_3 with H-4″, and the quaternary carbon at C-2″ (δ_C 117.5). The ^{13}C NMR data (Table 2) corroborated these findings, displaying 45 carbon signals in alignment with the ^{1}H NMR and HSQC spectra.

The linkage between the 2,7-dihydroxy-4-methoxy-9,10-dihydrophenanthrene-1,6-yl unit and the 5″,3‴-dihydroxy-3″-methoxybibenzyl-2″-yl moiety at C-6 and C-2″ was established through HMBC correlation from H-5 to C-2″, complemented by the NOESY interaction between H-5 and H-7″. However, the connection between the 2,7-dihydroxy-4-methoxy-9,10-dihydrophenanthrene-1,6-yl moiety and the 2′,7′-dihydroxy-4′-methoxy-9′,10′-dihydrophenanthrene-1′-yl unit could not be unequivocally determined through HMBC and NOESY correlations due to the quaternary carbon's chemical environment. Nonetheless, assignments of the proton and carbon signals based on 2D NMR data, along with the identification of the dimerization sites at C-1 and C-1′, were supported. This was further corroborated by the comparison of the similar carbon chemical shifts at C-1 (δ_C 117.4) and C-1′ (δ_C 116.6) with those reported for blestriarene A [22]. As a result, the planar structure of compound **1** was constructed as a novel 9,10-dihydrophenanthrene/bibenzyl trimer.

Atropisomerism, arising from restricted rotation around a single bond, results in isomers (atropisomers) with distinct bioactivities and toxicities, impacting drug development significantly. Compound **1**, with its characteristic biphenyl structure, is predisposed to forming atropisomers due to intramolecular steric hindrance. It was identified as a racemate, as evidenced by the split proton and carbon signals, such as δ_H 6.55/6.54 (H-3) and δ_C 122.2/122.1 (C-6), and an optical rotation value approximating zero. As previously discussed [21], 9,10-dihydrophenanthrene-type monomers are regarded as optically pure entities because their rotational energy barriers, ranging between 3 kcal·mol^{-1} and 5 kcal·mol^{-1}, fall well below the atropisomerism threshold of 20 kcal·mol^{-1} (Fig. 4A). Chiral HPLC analysis demonstrated that compound **1** exhibited four distinct chromatographic peaks, indicating the presence of two chiral axes (*a* and *a*′) at C_1-$C_{1'}$ and C_6-$C_{2''}$, respectively. However, the four stereoisomers of compound **1** could not be isolated as distinct entities in solution, even under dark conditions. Compounds **1a$_1$** and **1a$_2$** (collectively **1a**) could rapidly interconvert, eventually stabilizing at a certain ratio, a behavior also observed for **1b$_1$** and **1b$_2$** (collectively **1b**). This phenomenon is interpreted through rotational energy barrier theory [23]: the rotational energy barrier for the C_1-$C_{1'}$ axis (*a*) was measured at 38.7 kcal/mol (Fig. 4B), exceeding the atropisomeric threshold of 30 kcal/mol and indicating two stable atropisomers for axis *a*. Conversely, the rotational energy barrier for the C_6-$C_{2''}$ axis (*a*′) was 22.3 kcal/mol, close to the low threshold of 20 kcal·mol^{-1}, suggesting that the atropisomers of axis *a*′ [23] rapidly interconvert. Therefore, while compounds **1a** and **1b** manifest as stable structures, their constituent stereoisomers (**1a$_1$**, **1a$_2$**, **1b$_1$**, and **1b$_2$**) could not be isolated as pure entities.

The 1D NMR data for compounds **1a** (comprising **1a$_1$** and **1a$_2$**) and **1b** (comprising **1b$_1$** and **1b$_2$**) were consistent with those of compound **1**, indicating that **1a** and **1b** are enantiomers. However, the observation of split NMR signals for protons and carbons in both **1a** and **1b** suggested that **1a$_1$** and **1a$_2$** are diastereomers of each other, as are **1b$_1$** and **1b$_2$**. A heating experiment further revealed that the ^{1}H NMR spectrum of compound **1** could transform to a single set of signals, rather than two distinct sets, upon heating to 120 °C in DMSO-d_6, suggesting reversible interconversion between the diastereomers under elevated temperatures (Supporting Information, Fig. S9). The optical rotation values and electronic circular dichroism (ECD) curves for compounds **1a** and **1b** confirmed their enantiomeric relationship. The optical rotation values were measured as −7.0 for **1a** and +6.0 for **1b** in methanol. Correspondingly, their ECD curves exhibited mirror-image Cotton effects near 225 nm, 250 nm, 280 nm, and 320 nm, underscoring their enantiomeric nature. The stereochemistry of **1a** and **1b** was definitively determined through comparison of experimental and calculated ECD curves, which revealed closely matching Cotton effects at the aforementioned wavelengths (Fig. 5A). As a result, compound **1**, including both **1a** and **1b**, was designated as (a*R*)- and (a*S*)-

Table 1 The compounds 1–5 were measured in 600 MHz (CD_3OD) for ^1H NMR data

No.	1 (1a, 1b)	2 (2a, 2b)	3 (3a, 3b)	4 (4a, 4b)	5I	5II
3	6.55/6.54 (s)	6.58/6.59 (s)	6.55 (s)	6.62 (s)	6.54 (s)	6.52 (s)
5	7.94/7.93 (s)	7.89/7.88 (s)	7.92/7.91 (s)	8.01 (s)	7.90 (s)	7.89 (s)
8	6.74/6.73 (s)	6.71 (s)	6.740/6.736 (s)	6.80 (s)	6.71 (s)	6.70 (s)
9	2.56 (m)	2.56 (m)	2.64 (m)	2.61 (m)	2.61 (m)	2.58 (m)
			2.50 (m)		2.57 (m)	
10	2.34 (m)	2.39 (m)	2.50 (m)	2.41 (m)	2.38 (m)	2.36 (m)
				2.27 (m)	2.32 (m)	
3′	6.59/6.58 (s)	6.54 (s)	6.58/6.57 (s)	6.95/6.94 (s)		
4′					6.40 (d, 2.4)	6.39 (d, 2.4)
5′	8.05/8.04 (d, 8.4)	8.055/8.048 (d, 8.4)	8.05 (d, 8.4)	9.46 (d, 9.0)		
6′	6.644/6.635 (dd, 8.4, 2.4)	6.64/6.63 (dd, 8.4, 2.8)	6.64/6.63 (dd, 8.4, 2.4)	7.10 (br d, 9.0)	6.41 (d, 2.4)	6.40 (d, 2.4)
7′					2.58 (m)	2.59 (m)
8′	6.62/6.61 (d, 2.4)	6.61/6.59 (d, 2.8)	6.62/6.60 (d, 2.4)	7.13/7.11 (dd, 9.0, 2.4)		
9′	2.56 (m)	2.56 (m)	2.55 (m)	7.44/7.41 (d, 9.0)		
10′	2.55 (m)	2.32 (m)	2.35 (m)	7.25/7.20 (d, 9.0)		
	2.50 (m)					
2″					6.40 (t, 2.4)	6.44 (t, 2.4)
3″			6.587/6.582 (s)	6.95 (s)		
4″	6.41/6.39 (d, 2.4)	6.392/6.394 (d, 2.4)			6.50 (dd, 7.8, 2.4)	6.49 (dd, 7.8, 2.4)
5″			8.05 (d, 8.4)	9.46 (d, 9.0)	6.95 (t, 7.8)	6.91 (t, 7.8)
6″	6.41 (d, 2.4)	6.37/6.36 (d, 2.4)	6.630/6.628 (dd, 8.4, 2.4)	7.10 (br d, 9.0)	6.40 (dd, 7.8, 2.4)	6.38 (br d, 7.8)
7″	2.58 (m)	2.65 (m)			2.58 (m)	2.53 (m)
8″			6.591/6.585 (d, 2.4)	7.14/7.13 (d, 2.4)		
9″			2.55 (m)	7.47/7.45 (d, 9.0)		
10″			2.35 (m)	7.52/7.49 (d, 9.0)		
2‴	6.40/6.39 (m)	6.42/6.41 (t, 2.0)				
4‴	6.51/6.49 (br d, 7.8)	6.48 (m)			6.40 (d, 2.4)	6.39 (d, 2.4)
5‴	6.95/6.94 (t, 7.8)	6.90/6.92 (t, 7.6)				
6‴	6.41/6.38 (m)	6.37 (br d, 7.6)			6.38 (d, 2.4)	6.35 (d, 2.4)
7‴	2.50 (m)	2.58, m			2.58 (m)	2.70, (m)
2⁗					6.41 (m)	6.45 (t, 1.8)
4⁗					6.48 (dd, 7.8, 2.4)	6.46 (dd, 8.4, 1.8)
5⁗					6.92 (t, 7.8)	6.85 (t, 8.4)
6⁗					6.364 (br d, 7.8)	6.363 (br d, 8.4)
7⁗					2.58 (m)	2.61 (m)
2-OCH_3		3.891/3.894 (s)	3.807 (s)	3.80 (s)		
4-OCH_3	3.82/3.81 (s)				3.77 (s)	3.74 (s)
2′-OCH_3		3.753/3.750 (s)	3.880 (s)	4.15 (s)		
3′-OCH_3					3.66 (s)	3.65 (s)
4′-OCH_3	3.89 (s)					
2″-OCH_3			3.888/3.886 (s)	4.15 (s)		
3″-OCH_3	3.67/3.64 (s)	3.686/3.694 (s)				
3‴-OCH_3					3.693 (s)	3.685 (s)

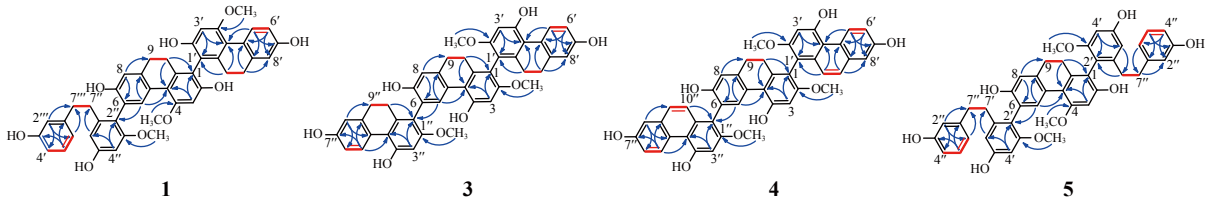

1 **3** **4** **5**

Fig. 2 The key HMBC (blue) and ^{1}H-^{1}H COSY (red) correlations of compounds 1 and 3–5.

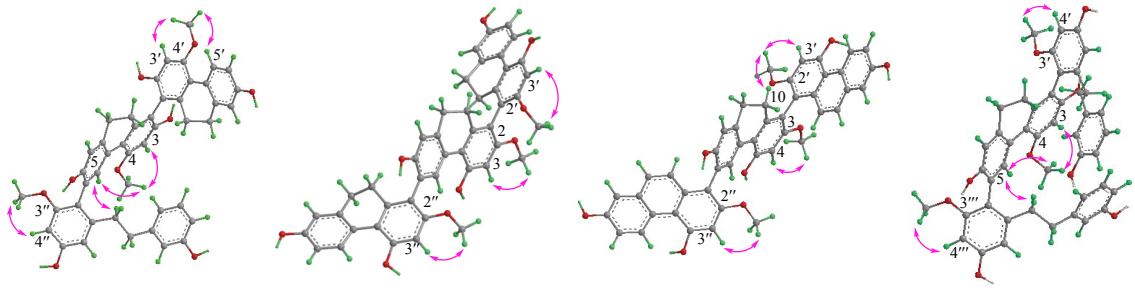

1 **3** **4** **5**

Fig. 3 The key NOESY correlations of compounds 1 and 3–5.

blephebibnol F, respectively.

Compound **2** was obtained as a yellowish amorphous powder. Its molecular formula of $C_{45}H_{40}O_9$ was established based on HRESIMS data showing an ion peak at *m/z* 725.2742 $[M + H]^+$, identical to that of compound **1**. Comparison of the NMR data of compound **2** (Tables 1 and 2) with those of compound **1** revealed highly similar structures, with the exception of the positions of methoxyl groups. HMBC cross-peaks from 2-OCH_3 to C-2 and from 2′-OCH_3 to C-2′, coupled with NOESY correlations of 2-OCH_3 with H-3 and 2′-OCH_3 with H-3′, indicated the placement of the methoxyl groups at C-2 and C-2′. The rotational energy barriers for the C_1-$C_{1'}$ and C_6-$C_{2''}$ axes in compound **2** were calculated to be 47.1 and 21.4 kcal·mol^{-1}, respectively, suggesting stereochemistry similar to that of compound **1** (Fig. 4B). Chiral HPLC purification yielded two structures **2a** and **2b**. The ECD curves calculated for these structures aligned well with the experimental data at 240, 270, and 315 nm (Fig. 5B). Consequently, compound **2**, including both **2a** and **2b**, was determined to be (a*R*)- and (a*S*)-blephebibnol G, respectively.

Compound **3** was isolated as a brown amorphous powder. Its molecular formula was determined to be $C_{45}H_{38}O_9$ based on the HRESIMS ion peak at *m/z* 721.2451 $[M - H]^-$, indicating a loss of two hydrogen atoms and an additional degree of unsaturation compared to compound **2**. The NMR data analysis for compound **3** (Tables 1 and 2) revealed similarities to those of compound **2**, with notable exceptions: three AMX system signals at δ_H 8.05 (H-5″, d, *J* =

Table 2 The compounds 1–5 were measured in 150 MHz (CD_3OD) for ^{13}C NMR data

No.	1 (1a, 1b)	2 (2a, 2b)	3 (3a, 3b)	4 (4a, 4b)	5I	5II
1	117.4, C	115.9, C	115.9, C	115.2, C	116.5, C	116.5, C
2	155.1, C	158.6, C	158.4, C	159.0, C	155.0, C	154.9, C
3	99.5, CH	99.3, CH	99.5, CH	99.5, CH	99.4, CH	99.4, CH
4	158.3, C	155.4, C	155.7, C	156.2, C	158.2, C	158.3, C
4a	118.5/118.4, C	117.7, C	118.5, C	117.8, C	117.5, C	117.7, C
4b	127.0/126.9, C	126.5, C	126.8, C	127.0, C	126.6, C	126.6, C
5	133.4, CH	133.5, CH	133.4, CH	134.3, CH	133.5, CH	133.5, CH
6	122.2/122.1, C	122.7, C	122.3, C	121.7, C	122.7, C	122.7, C
7	154.0/153.9, C	153.8, C	154.1, C	154.6, C	153.8, C	153.7, C
8	115.3, CH	115.0, CH	115.4, CH	115.6, CH	115.0, CH	114.9, CH
8a	140.4/140.3,C	139.9, C	140.3, C	140.6, C	139.9, C	139.8, C
9	31.0, CH_2	30.9, CH_2	30.9, CH_2	31.0, CH_2	31.0, CH_2	31.0, CH_2
10	28.6, CH_2	28.5, CH_2	29.0, CH_2	28.6/28.5, CH_2	28.7, CH_2	28.6, CH_2
10a	141.7/141.6, C	141.9, C	141.4, C	142.6, C	141.6, C	141.7, C
1′	116.6, C	115.8, C	115.9, C	112.5, C	145.0, C	144.8, C
2′	155.2, C	158.7, C	158.6, C	160.1, C	117.7, C	117.5, C
3′	99.4, CH	99.4, CH	99.4, CH	100.6, CH	160.4, C	160.6, C
4′	158.3, C	155.5, C	155.7, C	154.2/154.1, C	98.5, CH	98.4, CH

Continued

No.	1 (1a, 1b)	2 (2a, 2b)	3 (3a, 3b)	4 (4a, 4b)	5I	5II
4′a	117.8/117.7, C	117.9, C	117.6, C	116.9, C		
4′b	126.7, C	126.7, C	126.7, C	125.8, C		
5′	130.5, CH	130.5, CH	130.5, CH	130.7, CH	158.7, C	159.0, C
6′	113.6, CH	113.6, CH	113.6, CH	117.4, CH	109.4, CH	109.5, CH
7′	156.2, C	156.2, C	156.2, C	155.5, C	37.8, CH_2	37.8, CH_2
8′	114.8, CH	114.9, CH	114.9, CH	112.2, CH		
8′a	141.1, C	141.0, C	141.0, C	134.7, C		
9′	31.3, CH_2	31.2, CH_2	31.3, CH_2	128.6, CH		
10′	29.1/29.0, CH_2	28.4, CH_2	28.4, CH_2	125.8, CH		
10′a	141.5/141.4, C	141.7, C	141.9, C	135.1/135.0, C		
1″	145.0/144.8, C	144.8, C	117.7, C	115.2, C	145.5, C	145.5, C
2″	117.5, C	120.1, C	158.6, C	160.4, C	116.3, CH	116.4, CH
3″	160.5, C	160.3, C	99.3, CH	100.4, CH	158.3, C	158.2, C
4″	98.3, CH	98.4, CH	155.6/155.5, C	153.6, C	113.7, CH	113.7, CH
4″a			117.6, C	116.9, C		
4″b			126.7, C	125.9, C		
5″	159.0, C	158.7, C	130.5, CH	130.7, CH	130.3, CH	130.4, CH
6″	109.4, CH	109.5, CH	113.6, CH	117.3, CH	120.9, CH	121.0, CH
7″	38.4, CH_2	38.1, CH_2	156.2, C	155.5, C	38.1, CH_2	38.2, CH_2
8″			114.8, CH	112.2, CH		
8″a			140.9, C	134.7, C		
9″			31.2, CH_2	128.1/128.2, CH		
10″			28.4, CH_2	126.6, CH		
10″a			141.8/141.7, C	134.9, C		
1‴	145.4, C	145.5, C			144.8, C	144.8, C
2‴	116.6/116.3, CH	116.42/116.39, CH			120.1, C	120.1, C
3‴	158.3, C	158.2, C			160.3, C	160.3, C
4‴	113.7, CH	113.6, CH			98.5, CH	98.3, CH
5‴	130.3, CH	130.2, CH			159.0, C	158.7, C
6‴	120.9/120.8, CH	121.0, CH			109.5, CH	109.4, CH
7‴	37.9, CH_2	38.6, CH_2			38.3, CH_2	38.5, CH_2
1⁗					145.4, C	145.4, C
2⁗					116.4, CH	116.3, CH
3⁗					158.31, C	158.25, C
4⁗					113.6, CH	113.7, CH
5⁗					130.2, CH	130.3, CH
6⁗					121.0, CH	120.9, CH
7⁗					38.6, CH_2	38.1, CH_2
2-OCH_3		56.1, CH_3	56.2, CH_3	56.2, CH_3		
4-OCH_3	56.3, CH_3				56.2, CH_3	56.3, CH_3
2′-OCH_3		56.2, CH_3	56.1, CH_3	56.2, CH_3		
3′-OCH_3					56.2, CH_3	56.1, CH_3
4′-OCH_3	56.1, CH_3					
2″-OCH_3			56.1, CH_3	56.2, CH_3		
3″-OCH_3	56.1, CH_3	56.3, CH_3				
3‴-OCH_3					56.3, CH_3	56.2, CH_3

8.4 Hz), 6.63 (H-6″, dd, J = 8.4, 2.4 Hz) and 6.591 (H-8″, d, J = 2.4 Hz) and one aromatic singlet at δ_H 6.587 (H-3″, d, J = 8.4 Hz) in compound **3**, replacing four aromatic protons at δ_H 6.42 (H-2‴, t, J = 2.0 Hz), 6.48 (H-4‴, m), 6.90 (H-5‴, t, J = 7.6 Hz), and 6.37 (H-6‴, br d, J = 7.6 Hz), and two aromatic meta-position protons at δ_H 6.392 (H-4″, d, J = 2.4 Hz) and 6.37 (H-6″, d, J = 2.4 Hz) of compound **2**. This difference indicated a substitution of the bibenzyl moiety in compound **2** with a 9,10-dihydrophenanthrene unit in compound **3**, as corroborated by HMBC correlations from H-3″ to C-1″ and C-4″a, from H-5″ to C-4″a, C-7″, and C-8″a, from H-8″ to C-4″b, C-6″, and C-9″, and from H-10″ to C-1″, alongside a ^{1}H-

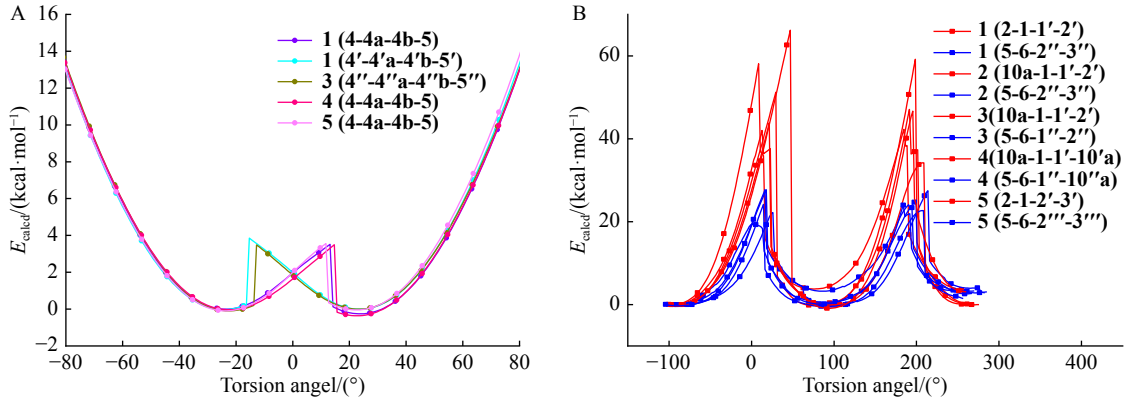

Fig. 4 (A) Quantum mechanics (QM) energy profiles are displayed for the torsion angles of 9,10-dihydrophenanthrene monomers of compounds 1 and 3–5. (B) QM energy profiles are displayed for the torsion angles of linkages between monomers of compounds 1–5. Their calculated dihedral angles are marked in brackets.

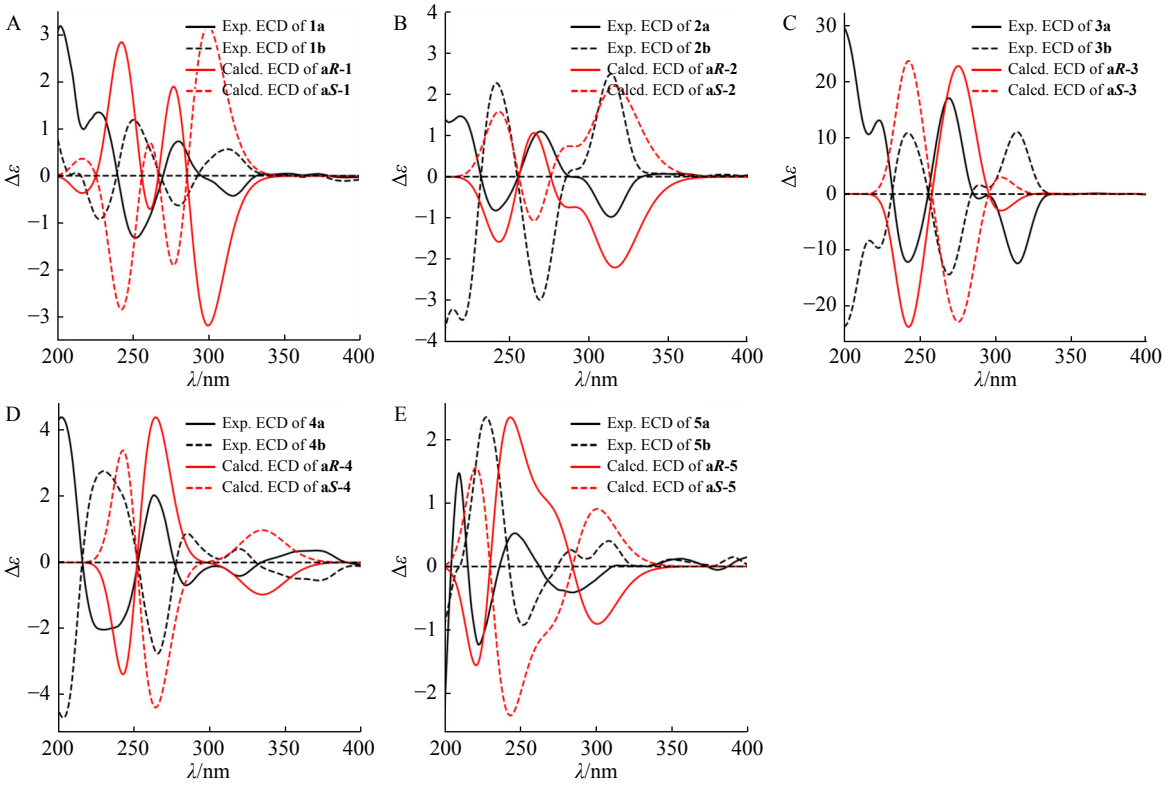

Fig. 5 Experimental and calculated ECD curves of compounds 1–5.

^{1}H COSY interaction between H-9″ with H-10″ (Fig. 2). Additionally, HMBC signals from 2″-OCH_3 to C-2″ and NOESY correlations between 2″-OCH_3 and H-3″ confirmed the placement of the methoxyl group at C-2″ (Fig. 3).

The HMBC signal from H-5 to C-1″, in conjunction with the quaternary carbons signals at C-6 (δ_C 122.3) and C-1″ (δ_C 117.7), elucidated the linkage between C-6 and C-1″. The calculated rotational energy barriers for the C_1-$C_{1'}$ and C_6-$C_{1''}$ axes of compound **3** were determined to 42.0 and 19.4 kcal/mol, respectively, indicating a stereochemistry akin to that observed in compound **1** (Fig. 4B). Chiral separation of compound **3** produced two atropisomers, **3a** and **3b**, which exhibited opposing Cotton effects in their ECD spectra. The configurations of these atropisomers were established as a*R* and a*S* through comparison of their experimental ECD curves with calculated ones, particularly at wavelengths near 245 nm, 270 nm, and 320 nm (Fig. 5C). Consequently, the structure of compound **3**, including its atropisomers **3a** and **3b**, was designated as (a*R*)- and (a*S*)-blephebibnol H, respectively.

Compound **4** was isolated as a brown amorphous powder with the molecular formula of $C_{45}H_{34}O_9$, determined by the HRESIMS ion peak at *m*/*z* 717.2139 $[M - H]^-$. This indicated a reduction of four hydrogen atoms and an increase of

two degrees of unsaturation compared to compound **3**. Examination of the ^{1}H NMR data for compound **4**, in comparison with those of compound **3** (Tables 1 and 2), revealed key differences. Notably, the presence of two sets of aromatic AB system protons at δ_H 7.44 (H-9′, d, J = 9.0 Hz), 7.25 (H-10′, d, J = 9.0 Hz), 7.47 (H-9″, d, J = 9.0 Hz), and 7.52 (H-10″, d, J = 9.0 Hz) in compound **4** , as opposed to four methylene signals at δ_H 2.55 (H_2-9′, m), 2.35 (H_2-10′, m), 2.55 (H_2-9″, m), and 2.35 (H_2-10″, m) in compound **3**, indicated the substitution of two 9,10-dihydrophenanthrene units with phenanthrene moieties in compound **4**. This substitution was further supported by additional aromatic carbon signals at δ_C 128.6 (C-9′), 125.8 (C-10′), 128.1 (C-9″), and 126.6 (C-10″). Moreover, HMBC correlations from 2-OCH_3 to C-2, from 2′-OCH_3 to C-2′, and from 2″-OCH_3 to C-2″ (Fig. 2), combined with NOESY cross-peaks of 2-OCH_3 with H-3, of 2′-OCH_3 with H-3′, and of 2″-OCH_3 with H-3″ (Fig. 3), suggested the positioning of these methoxyl groups at C-2, C-2′, and C-2″, respectively.

The calculated rotational energy barriers for the axes C_1-$C_{1'}$ and C_6-$C_{1''}$ of compound **4** were 34.2 and 19.9 kcal/mol, respectively, indicating a stereochemistry similar to that of compound **1** (Fig. 4B). Chiral HPLC separation of compound **4** resulted in two atropisomers, **4a** and **4b**, exhibiting opposite Cotton effects. Their configurations were determined as a*R* and a*S*, based on the comparison of calculated and experimental ECD curves near 230 nm, 260 nm, and 330 nm (Fig. 5D). Consequently, the structure of compound **4**, including **4a** and **4b**, was elucidated as (a*R*)- and (a*S*)-blephebibnol I, respectively.

Compound **5** was isolated and identified through a process distinct from that used for compounds **1**–**4**. Achiral HPLC separation of compound **5** yielded two splitting chromatographic peaks, **5I** and **5II** (Supporting Information, Fig. S2E). Compound **5I** was obtained as a yellowish amorphous powder, with its molecular formula established as $C_{45}H_{42}O_9$ based on HRESIMS data at *m/z* 727.2899 $[M + H]^+$, indicating an increase of two hydrogen atoms compared to compound **1**. The ^{1}H NMR spectrum of **5I** (Table 1) showed similarities to that of compound **1**, with the exception of two additional aromatic signals at δ_H 6.41 (H-6′, d, J = 2.4 Hz) and 6.40 (H-6″, dd, J = 7.8, 2.4 Hz). These signals suggested the replacement of a 9,10-dihydrophenanthrene unit in compound **1** with a bibenzyl moiety in **5I**. This substitution was confirmed by HMBC correlations from H-4′ to C-2′ and C-6′, from H-6′ to C-7′, from H-7′ to C-2′, from H-4″ to C-2″ and C-6″, from H-5″ to C-1″ and C-3″, from H-6″ to C-7″, from H-7″ to C-2″, and from 3′-OCH_3 to C-3′, combined with a ^{1}H-^{1}H COSY correlation between H-7′ and H-7″ (Fig. 2) and a NOESY signal of 3′-OCH_3 with H-4′ (Fig. 3). The connectivity between the additional bibenzyl moiety and the 9,10-dihydrophenanthrene unit was inferred to be at C-1 and C-2′, as indicated by the quaternary carbon signals at C-1 (δ_C 116.5) and C-2′ (δ_C 117.7). Compound **5II** was determined to share the same planar structure as **5I**, as confirmed by HRESIMS and NMR data (Tables 1 and 2).

Further investigations revealed that compounds **5I** and **5II** were unable to maintain chiral stability, even in a dark environment, and interconverted within three days. The calculated rotational energy barriers for the axes C_1-$C_{2'}$ and C_6-$C_{2'''}$ of compound **5** were 43.5 and 22.5 kcal·mol^{-1}, respectively, highlighting the instability of the chiral axis *a*′. Chiral HPLC separation of compound **5** resulted in the isolation of compounds **5a** and **5b** (Supporting Information, Fig. S2F). Their configurations were determined to be a*R* and a*S*, respectively, based on the comparison of calculated and experimental ECD curves near 225 nm, 250 nm, and 300 nm (Fig. 5E). Consequently, the structure of compound **5**, including **5a** and **5b**, was elucidated as (a*R*)- and (a*S*)-blephebi bnol J.

Additionally, two known compounds were identified as blestrin A [24] and blestrin D [25] by comparing their NMR and ESIMS data with those reported in the literature.

The biogenetic origins of compounds **1**–**5** are derived from dihydro-*m*-cinnamoyl-CoA, the precursor of monomer **i** Scheme 1 [11]. This precursor undergoes intramolecular free radical cyclization at either two para-positions or both ortho- and para-positions, leading to the formation of dihydrophenanthrene monomers **ii** and **ii′**. Subsequent dehydrogenation of monomer **ii** yields the phenanthrene monomer **iii**. Intermolecular free radical coupling reactions then occur between various combinations of these monomers: **ii′** with **ii′**, **ii** with **ii**, **iii** with **ii**, and **ii′** with **i**, resulting in intermediates **A**–**D**. The structures of compounds **1**–**5** are finalized through further intermolecular free radical couplings involving **A** with **i**, **B** with **i**, **B** with **ii**, **C** with **iii**, and **D** with **i**.

To evaluate the potential of these compounds as inhibitors of neuroinflammation, all were tested for their ability to inhibit LPS-induced nitric oxide (NO) production in BV-2 microglial cells. To ascertain whether the observed inhibitory effects on NO production were due to cytotoxicity, the viability of BV-2 cells was assessed using the MTT assay. As depicted in the results (Fig. 6), compounds **5b** and **6** demonstrated significant inhibitory effects on NO production, with IC_{50} values of 12.59 ± 0.40 and 15.59 ± 0.83 μmol·L^{-1}, respectively, without displaying notable cytotoxicity. For comparison, curcumin, employed as a positive control, showed an IC_{50} value of 2.57 ± 0.02 μmol·L^{-1}.

Compounds **5b** and **6** were subsequently assessed for their impact on inducible nitric oxide synthase (iNOS), a key enzyme that amplifies NO production during neuroinflammatory responses. LPS treatment significantly elevated the mRNA expression of iNOS compared to the control group. However, pre-treatment with compounds **5b** or **6** significantly inhibited the mRNA expression of iNOS in a dose-dependent manner in LPS-stimulated BV-2 cells, as demonstrated in the experimental results (Figs. 7A and 7B). Furthermore, pre-treatment with compounds **5b** or **6** also notably reduced the protein expression levels of iNOS at three different concentrations, aligning with the observed changes in mRNA expression (Figs. 7C and 7D). This correlation between

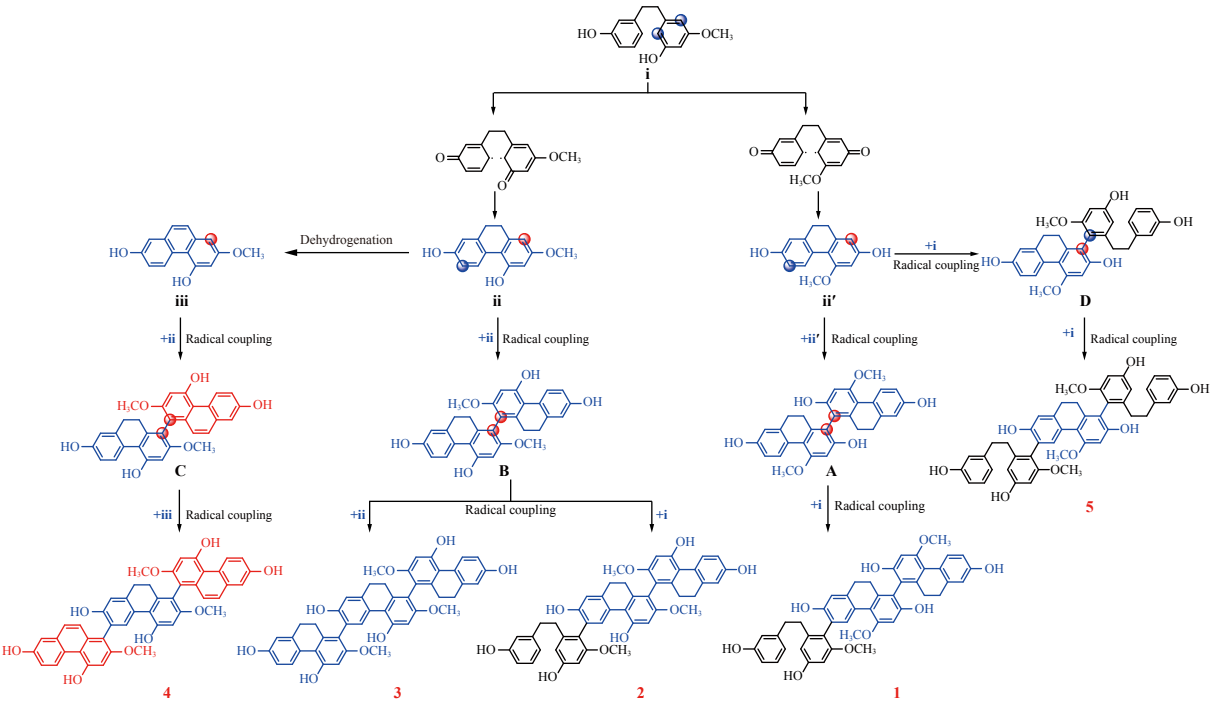

Scheme 1 Possible biosynthetic pathway of compounds 1–5.

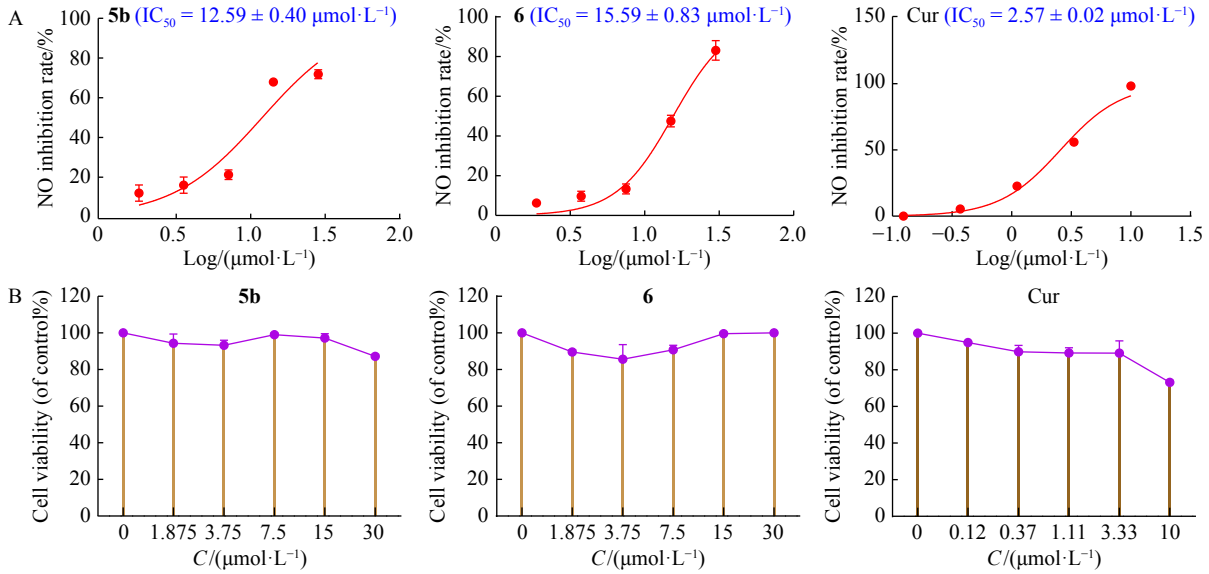

Fig. 6 The NO inhibition rates of 5b, 6, and the positive control curcumin (Cur) and the cell viability of 5b, 6, and curcumin (Cur) treated BV-2 cells. Data are the mean ± SD, *n* = 3.

mRNA and protein expression levels provides additional evidence of the anti-inflammatory potential of these compounds in neuroinflammatory contexts.

The overexpression of inducible nitric oxide synthase (iNOS) is often triggered by the activation of nuclear factor kappa-B (NF-κB), a central mediator in neuroinflammation. AKT and IκB are two primary upstream proteins involved in the activation process of NF-κB. To investigate the potential neuroinflammatory modulation by compounds **5b** and **6**, their effects on the expression levels of NF-κB, phosphorylated NF-κB (p-NF-κB), IκBα, phosphorylated IκBα (p-IκBα), AKT, and phosphorylated AKT (p-AKT) were assessed. The results indicated that both compounds **5b** and **6** significantly reduced the phosphorylation of NF-κB at all tested concentrations in LPS-induced BV-2 microglial cells (Figs. 7C and 7D). Moreover, at higher concentrations, these compounds also diminished the phosphorylation levels of IκBα and AKT. These findings suggest that compounds **5b** and **6** may mitigate the neuroinflammatory response in LPS-stimulated BV-2 cells by inhibiting the phosphorylation of NF-κB, IκBα, and AKT.

PTP1B has recently been identified as a crucial regulator

in microglia-mediated neuroinflammation [6]. In light of this, all compounds were evaluated for their PTP1B inhibitory activities, revealing that compounds **3a**, **6**, and **7** exhibited significant inhibitory effects, with percentages of inhibition at 86.3%, 89.1%, and 84.7%, respectively. These results were comparable to the positive control CCF06240, which showed an inhibition rate of 101.9%. (Supporting Information, Table S2). Further investigation through dose-response studies provided IC_{50} values for compounds **3a**, **6**, and **7** of 1.52 ± 0.34, 1.39 ± 0.11, and 1.78 ± 0.01 μmol·L^{-1} (Fig. 8), respectively, versus the positive control CCF06240 with an IC_{50} of 1.70 μmol·L^{-1} [18]. To explore the molecular basis for the observed PTP1B inhibitory activity, molecular docking calculations were conducted using the PM6 model. This analysis indicated that the (9,10-dihydro)phenanthrene/bibenzyl derivatives may exert their PTP1B inhibitory effect through a combination of hydrogen bonding, π-π stacking, hydrophobic interactions, and π-cation interactions (Fig. 8).

Compound **3a**, a novel 9,10-dihydrophenanthrene trimer, was further investigated for its biological activity. The viability of BV-2 cells treated with compound **3a** was assessed through the MTT method, revealing no significant cytotoxic effects (Fig. 9A). Exposure to LPS notably increased the mRNA expression levels of TNF-α and IL-1β in BV-2 cells, serving as indicators of neuroinflammation, compared to the control group. However, pre-treatment with compound **3a** significantly mitigated the LPS-induced upregulation of TNF-α in a dose-dependent manner. Moreover, the pre-treatment with **3a** at the highest concentration also reduced the mRNA expression level of IL-1β (Figs. 9B and 9C)

PTP1B overexpression in microglia activated by LPS can intensify the neuroinflammatory response through the activation of the NF-κB signaling pathway [6]. The impact of compound **3a** on the expression levels of NF-κB and IκBα was investigated to understand its anti-inflammatory mechanism. Following LPS treatment, there was a noticeable increase in the phosphorylation of NF-κB compared to the control group. Pre-treatment with compound **3a** significantly reduced the phosphorylation level of NF-κB at three different concentrations in LPS-stimulated BV-2 cells (Fig. 9D). However, **3a** pre-treatment did not markedly affect the phosphorylation of IκBα. (Fig. 9D). Based on these findings, it is hypothesized that compound **3a** mitigates LPS-induced neuroinflammation by inhibiting PTP1B activation and subsequently downregulating NF-κB phosphorylation. This leads to a decreased expression of pro-inflammatory factors, such as TNF-α and IL-

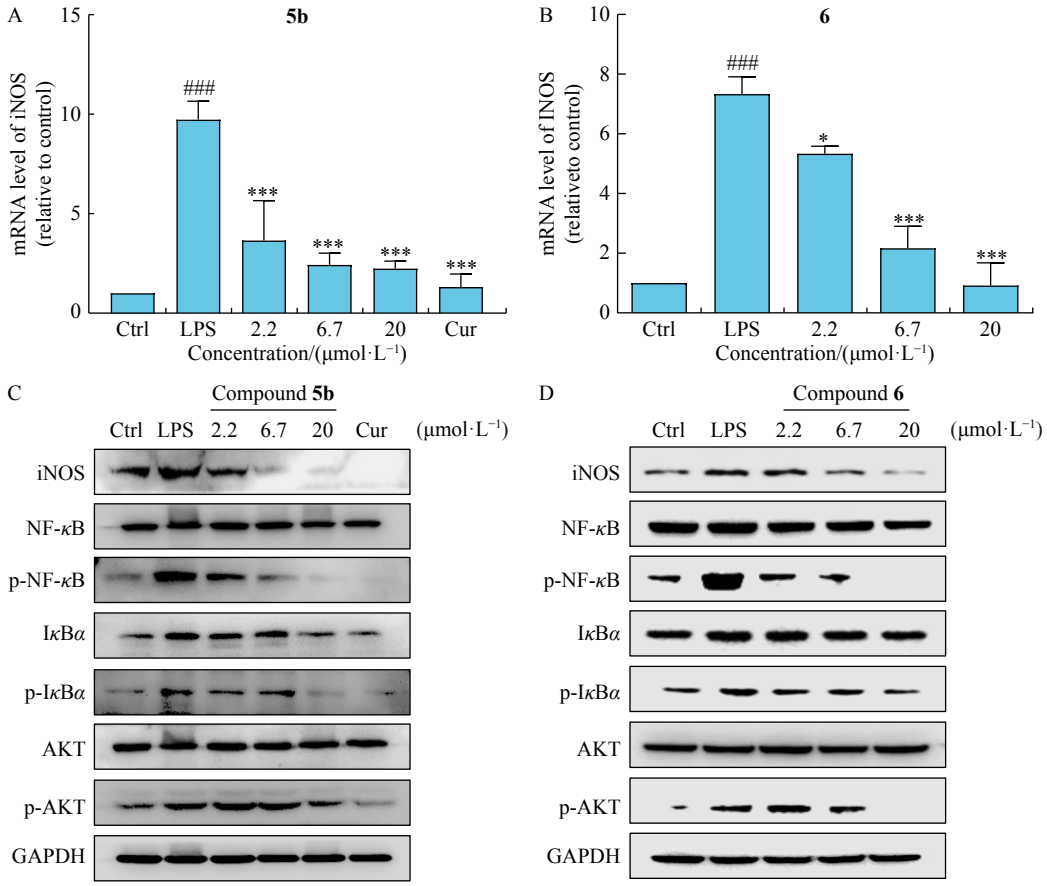

Fig. 7 Anti-neuroinflammatory activity of 5b and 6 in LPS-induced BV-2 cells. (A, B) Effects of 5b (A) and 6 (B) on the mRNA expression of iNOS. (C, D) Effects of 5b (C) and 6 (D) on the expression of iNOS, NF-κB p65, p-NF-κB p65, IκBα, p-IκBα, AKT, and p-AKT. GAPDH was the control for protein loading. Curcumin (Cur) was used as the positive control. Data are the mean ± SD, $n = 3$. $^{###}P < 0.001$, LPS *vs* Control; $^{*}P < 0.05$ and $^{***}P < 0.001$, LPS + samples *vs* LPS.

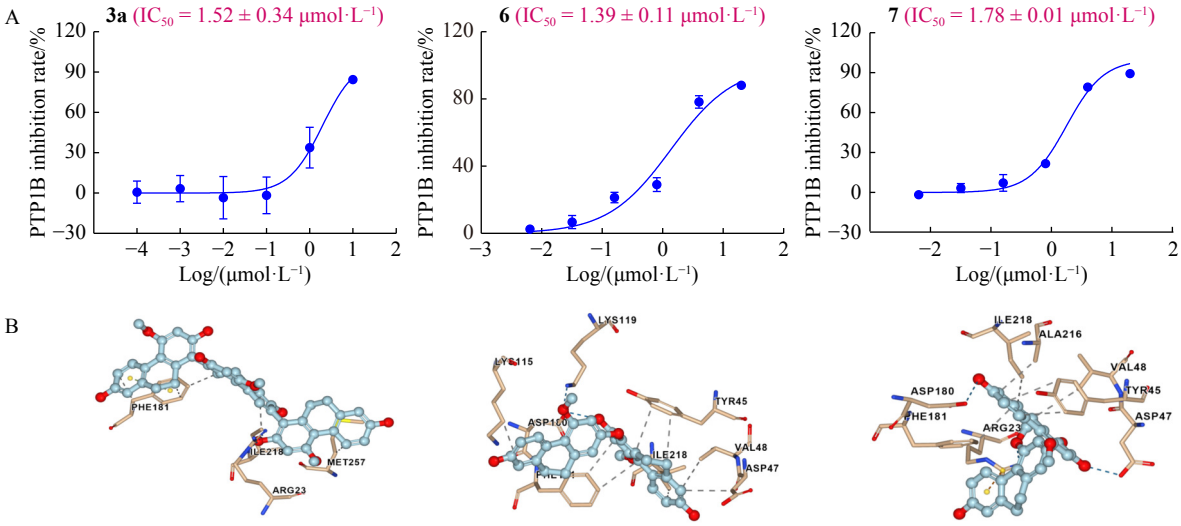

Fig. 8 PTP1B inhibitory effects of 3a, 6, and 7 and their 3D docked binding models with PTP1B. Data are the mean ± SD (n = 3). Blue, green, gray, and orange dashed lines indicate hydrogen bond, π-π stacking, hydrophobic interaction, and π-cation interaction, respectively.

1β, suggesting a potential therapeutic approach to modulate neuroinflammatory responses.

Conclusions

To identify potential therapeutics for neuroinflammation, five novel (9,10-dihydro)phenanthrene/bibenzyl trimers and two known compounds were isolated from the tubers of *Bletilla striata*. Bioactivity assessments demonstrated their significant inhibitory effects on NO production and PTP1B activity. Subsequent mechanistic studies indicated that these phenanthrene/bibenzyl derivatives could mitigate the expression of pro-inflammatory mediators by inhibiting the NF-κB signaling pathway (Fig. 10). These promising results suggest that phenanthrene/bibenzyl derivatives hold potential as lead

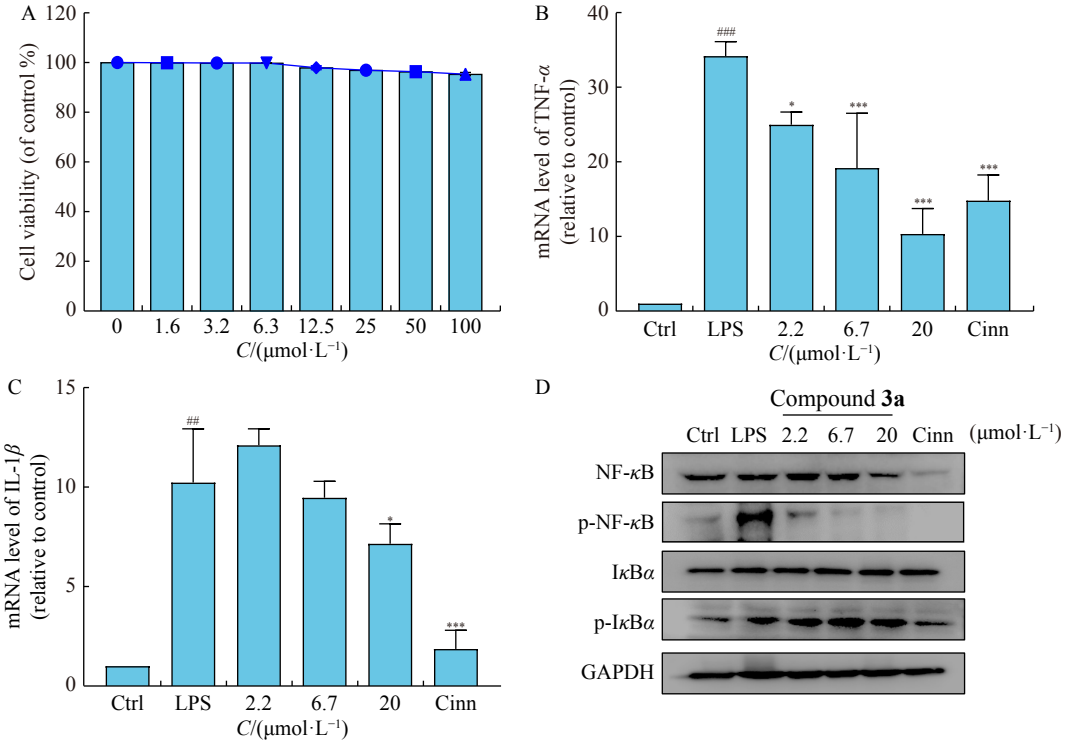

Fig. 9 Anti-neuroinflammatory activity of compound 3a in LPS-induced BV-2 cells. (A) The BV-2 cell viability after treating by different concentrations of 3a. (B, C) Effects of 3a on the mRNA expression of TNF-α and IL-1β. (D) Effects of 3a on the expression of NF-κB p65, p-NF-κB p65, IκBα, and p-IκBα. GAPDH was used as control for protein loading. CinnGEL 2Me (Cinn) was used as the positive control. Data are the mean ± SD (n = 3). $^{\#\#}P < 0.01$ and $^{\#\#\#}P < 0.001$, LPS *vs* Control; $^{*}P < 0.05$ and $^{***}P < 0.001$, LPS + samples *vs* LPS.

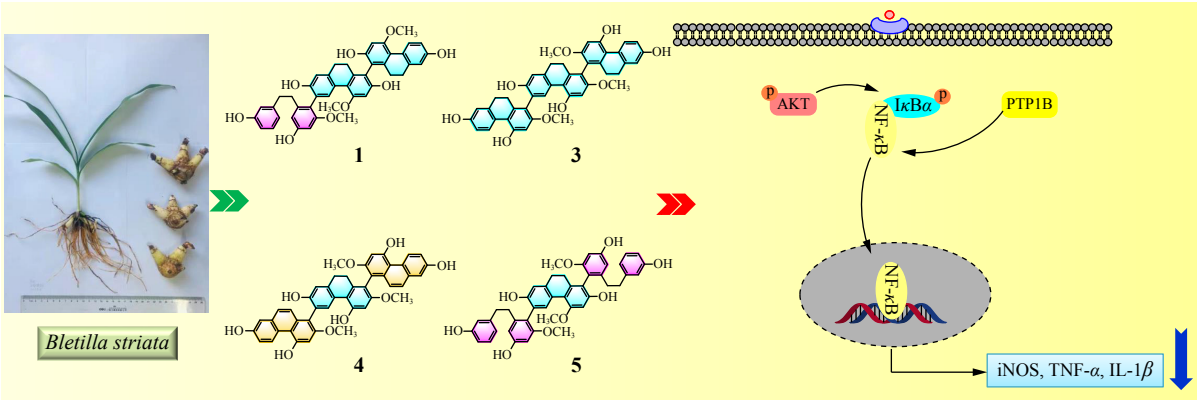

Fig. 10 Schematic diagram of anti-neuroinflammatory effects and underlying mechanisms of phenanthrene/bibenzyl trimers from *B. striata*.

compounds for developing treatments against neuroinflammation.

References

[1] Saha S, Buttari B, Profumo E, *et al*. A perspective on Nrf2 signaling pathway for neuroinflammation: a potential therapeutic target in Alzheimer's and Parkinson's diseases [J]. *Front Cell Neurosci*, 2022, **15**: 787258.

[2] Lei LY, Wang RC, Pan YL, *et al*. Mangiferin inhibited neuroinflammation through regulating microglial polarization and suppressing NF-κB, NLRP3 pathway [J]. *Chin J Nat Med*, 2021, **19**(2): 112-119.

[3] Xu XJ, Long JB, Jin KY, *et al*. Danshen-Chuanxiongqin Injection attenuates cerebral ischemic stroke by inhibiting neuroinflammation *via* the TLR2/TLR4-MyD88-NF-κB pathway in tMCAO mice [J]. *Chin J Nat Med*, 2021, **19**(10): 772-783.

[4] Ji WL, Liang K, An R, *et al*. Baicalin protects against ethanol-induced chronic gastritis in rats by inhibiting Akt/NF-κB pathway [J]. *Life Sci*, 2019, **239**: 117064.

[5] Wen J, Zhang YQ, Liu DQ, *et al*. Demethylenetetrahydroberberine protects dopaminergic neurons in a mouse model of Parkinson's disease [J]. *Chin J Nat Med*, 2022, **20**(2): 111-119.

[6] Vieira MNN, Silva NML, Ferreira ST, *et al*. Protein tyrosine phosphatase 1B (PTP1B): a potential target for Alzheimer's therapy [J]. *Front Aging Neurosci*, 2017, **9**: 7.

[7] Zabolotny JM, Kim YB, Welsh LA, *et al*. Protein-tyrosine phosphatase 1B expression is induced by inflammation *in vivo* [J]. *J Biol Chem*, 2008, **283**: 14230-14241.

[8] Song GJ, Jung M, Kim JH, *et al*. A novel role for protein tyrosine phosphatase 1B as a positive regulator of neuroinflammation [J]. *J Neuroinflamm*, 2016, **13**: 86.

[9] Newman DJ, Cragg GM. Natural products as sources of new drugs over the nearly four decades from 01/1981 to 09/2019 [J]. *J Nat Prod*, 2020, **83**: 770-803.

[10] Chinese Pharmacopoeia Commission. *Pharmacopoeia of the People's Republic of China* [M]. China Medical Science Press, 2015, **1** : 103.

[11] Sun MH, Ma XJ, Shao SY, *et al*. Phenanthrene, 9, 10-dihydrophenanthrene and bibenzyl enantiomers from *Bletilla striata* with their antineuroinflammatory and cytotoxic activities [J]. *Phytochemistry*, 2021, **182**: 112609.

[12] Lee JW, Kim JG, Lee D, *et al*. A new bibenzyl and a new methylflavan from the tubers of *Bletilla striata* [J]. *Phytochem Lett*, 2021, **44**: 149-153.

[13] Yang L, Peng C, Meng CW, *et al*. A new macrolide and six cycloartane triterpenoids from the tubers of *Bletilla striata* [J]. *Biochem Syst Ecol*, 2014, **57**: 238-241.

[14] Wang W, Meng H. Cytotoxic, anti-inflammatory and hemostatic spirostane-steroidal saponins from the ethanol extract of the roots of *Bletilla striata* [J]. *Fitoterapia*, 2015, **101**: 12-18.

[15] Jiang S, Wan K, Lou HY, *et al*. Antibacterial bibenzyl derivatives from the tubers of *Bletilla striata* [J]. *Phytochemistry*, 2019, **162**: 216-223.

[16] Wang DW, Wu F, Zhu YN, *et al*. Stilbene derivatives from the leaves and stems of *Bletilla striata* and their cytotoxicity and autophagy activity [J]. *Chem Nat Compd*, 2021, **57**: 462-467.

[17] LuT. Molecules program, Version 1.8.9, http://www.keinsci.com/research/molclus.html (accessed Oct 1st, 2019).

[18] Ma YM, Tao RY, Liu Q, *et al*. PTP1B inhibitor improves both insulin resistance and lipid abnormalities *in vivo* and *in vitro* [J]. *Mol Cell Biochem*, 2011, **357**: 65-72.

[19] Lang PT, Brozell SR, Mukherjee S, *et al*. Dock 6: combining techniques to model RNA-small molecule complexes [J]. *RNA*, 2009, **15**: 1219-1230.

[20] Mukherjee S, Balius TE, Rizzo RC. Docking validation resources: Protein family and ligand flexibility experiments [J]. *J Chem Inf Model*, 2010, **50**: 1986-2000.

[21] Sun MH, Ma XJ, Shao SY, *et al*. Atropisomeric 9, 10-dihydrophenanthrene/bibenzyl trimers with anti-inflammatory and PTP1B inhibitory activities from *Bletilla striata* [J]. *Org Biomol Chem*, 2022, **20**: 4736.

[22] Yamaki M, Bai L, Inoue K, *et al*. Bipheanthrenes from *Bletitla Striata* [J]. *Phytochemistry*, 1989, **28**: 3503-3505.

[23] LaPlante SR, Edwards PJ, Fader LD, *et al*. Revealing atropisomer axial chirality in drug discovery [J]. *ChemMedChem*, 2011, **6**: 505-513.

[24] Bai L, Yamaki M, Inoue K, *et al*. Blestrin A and B, bis(dihydrophenanthrene)ethers from *Bletilla striata* [J]. *Phytochemistry*, 1990, **29**: 1259-1260.

[25] Yamaki M, Bai L, Kato T, *et al*. Bisphenanthrene ethers from *Bletilla Striata* [J]. *Phytochemistry*, 1992, **31**: 3985-3987.

Cite this article as: SHAO Siyuan, SUN Mohan, MA Xianjie, *et al*. Novel phenanthrene/bibenzyl trimers from the tubers of *Bletilla striata* attenuate neuroinflammation *via* inhibition of NF-κB signaling pathway [J]. *Chin J Nat Med*, 2024, **22**(5): 441-454.